CFD Studies on Wind Turbine Interactions with the Turbulent Local Flow Field Influenced by Complex Topography and Thermal Stratification

Patrick Letzgus[1], Giorgia Guma[1], and Thorsten Lutz[1]

[1]Institute of Aerodynamics and Gas Dynamics, University of Stuttgart, Pfaffenwaldring 21, 70563 Stuttgart, Germany

Correspondence: Patrick Letzgus (patrick.letzgus@iag.uni-stuttgart.de)

Abstract. This paper shows the results of CFD studies of turbulent flow fields and their effects on a wind turbine in complex terrain. As part of the WINSENT project a research test site comprising four meteorological masts and two research wind turbines is currently being constructed in the Swabian Alps in Southern Germany. This work is an essential part of the research of the Southern German wind energy research cluster WindForS. The terrain site

5   is characterised by a densely forested escarpment and a flat plateau downstream of the slope. The met masts and wind turbines are built on this plateau.

In the first part, high-resolution CFD simulations are performed to separately investigate the effects of the forested escarpment and of thermal stratification on the flow field and on the wind turbine accordingly. In the second part, all the examined effects are combined for a real-life case dated March 2021. There, unstable conditions prevailed and

10   the forest shows low leaf area densities due to the wintertime.

It is shown that atmospheric turbulence, forests, orographies, and thermal stratification must be considered when assessing the impact of wind turbines in complex terrain. All of these effects influence the flow field both at the turbine position as well as in its wake. Turbulent structures of the forest wake cross the rotor plane temporarily and thereby affect the turbine inflow. Moreover, convective conditions and upward flows caused by the orography have

15   an impact on the performance output as inclined flows result in asymmetric torque distributions. The wind turbine wake and the forest wake mix further downstream, resulting in a fast decay of the turbine wake. The paper also describes how the turbulent flow in the wake changes in the presence of thermal stratification.

1 Introduction

In terms of wind turbine site assessment, complex topographies remain a major challenge. Because some research

20   questions on this topic are still unanswered, the importance of these investigations has been recognised for many years. Wegley et al. (1980) evaluated wind fields in complex terrain and demonstrated that orography-related over-speed of the wind is conducive to the beneficial use of wind energy. Using Reynolds-Averaged Navier-Stokes (RANS) methods, the over-speed and inclination can be mapped well (Brodeur and Masson, 2008). Lattice Boltzmann
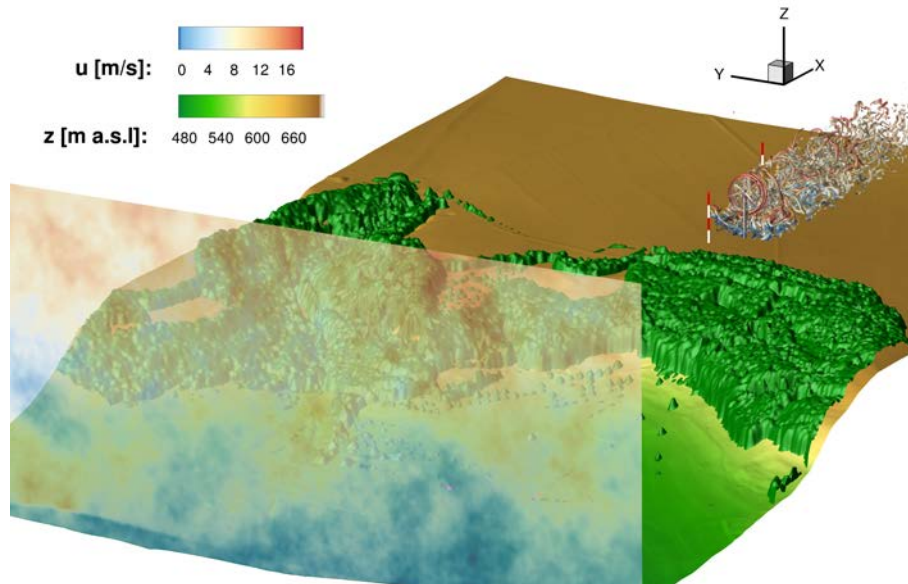
Figure 1. Overview of the numerical flow situations in the test field. In addition to the orography and the turbulent inflow plane, the wind turbine and its interaction with the flow field was also highlighted by λ_2 vortex structures

methods ~~are successfully~~ used to simulate wind fields in complex terrain (Schubiger et al., 2020). With hybrid RANS
25 and Large Eddy Simulation (LES) methods, even small vortices detached from the ground are resolved, increasing the accuracy of the simulations of the turbulent flow field in complex terrain (Bechmann and Sørensen, 2010). These hybrid RANS/LES methods are required for high-fidelity evaluations, because topographic effects such as forests and meteorological effects such as thermal stratification have a significant influence on the turbulent flow field. Delayed Detached Eddy Simulations (DDES) suit well for detailed wind turbine applications (Weihing et al., 2018).
30 Forests in complex topographies were analysed in a large-scale numerical LES study by Belcher et al. (2012a). They noted that forested hills have a more significant impact on the flow situation compared to forest flows in flat terrain. ~~Besides,~~ they explained that thermal stratification also has a strong influence on the resulting flow field. Belcher et al. (2012b) concluded that forested orographies downstream of the escarpment are more prone to flow separation than orographies without forest cover. Ivanell et al. (2018) conducted a numerical study to compare different simulation
35 methods to experimental data in forested complex terrain, and to evaluate their suitability for such conditions. As a result of their study, Desmond et al. (2017) found that thermal stratification also impacts the wake of forests and that turbulent kinetic energy changes fundamentally with thermal stability. The importance of considering all these topographic and meteorological phenomena in complex terrain has been confirmed by Finnigan et al. (2020), who have analysed the research and developments in this field over the last decades.

40 Murphy et al. (2020) examined that the orography- and thermal stability-related shear of the wind profile leads to a discrepancy of up to 5% in power generation and should therefore be accurately captured by measurements and simulations. Radünz et al. (2021) have identified the influence of local orographic effects and thermal stability on wind turbine wakes. It becomes apparent that these are also determinants of the performance output of wind turbines or complete wind farms. Barthelmie et al. (2018) conducted a study to investigate wind turbine wakes in Perdigão in

45 mountainous terrain and discovered that they strongly depend on topography and stability. Thermal stratifications have led to fundamental differences in wake trajectory measurements. The wake follows the orography more for stable conditions and less for unstable or neutral conditions. For convective conditions, the wake drifts upwards. The fact that thermal stability has a significant effect on the wake was also emphasised in the study by Abkar et al. (2016).

50 The WindForS project WINSENT attempts to overcome the challenges to predict more accurately the effects of complex terrain on wind turbines by establishing a test site on the Swabian Alps in Southern Germany. Four meteorological (met) masts and two research wind turbines are under construction. Thus, a variety of studies are conducted experimentally and numerically. The test field has already been analysed in other studies within the framework of this project. In coarser URANS studies over longer simulation periods, El Bahlouli et al. (2020) and

55 Berge et al. (2021) compared two selected days to Unmanned Aerial System (UAS) measurements.
This paper deals with highly resolved Computational Fluid Dynamics (CFD) simulations of the flow field at the test site in complex terrain and consequently on the wind turbine. In this work, new findings are presented that expand on previous studies of Schulz et al. (2016) and will provide more precise insights into the flow situation.
Figure 1 shows the entire wind energy test field. Besides the forested orography, the plot also depicts the turbulent

60 inflow plane. The fully meshed wind turbine has been integrated in its designated position and λ_2 vortex structures show the strong interactions of the ambient turbulence and the forest wake with the wind turbine wake. The two already existing met masts at the test site are marked. The setup that serves as a basis for these numerical simulations is explained in the following chapter. Dividing the results chapters into two parts will enhance the understanding of the emerging effects. The first part will explain the general effects on the flow field. This includes the characteristics

65 of the studied orography, the local forest, and thermal stratification. The investigations will show which influence the respective parameter reveals on the flow field. Subsequently, the effects will be applied separately to the wind turbine. This study will describe the complex conditions and simplify the interpretation of the flow field. The second part will then combine all effects based on real conditions of 10 March 2021. Considering all phenomena explained before, the flow field is then simulated and the behaviour on the wind turbine performance and its wake will be

70 analysed. The simulations are validated with experimental data of one meteorological (met) mast.

2 Setup

In the following, the numerical setup for the performed simulations in this work will be presented.

2.1   Terrain Site & Mesh
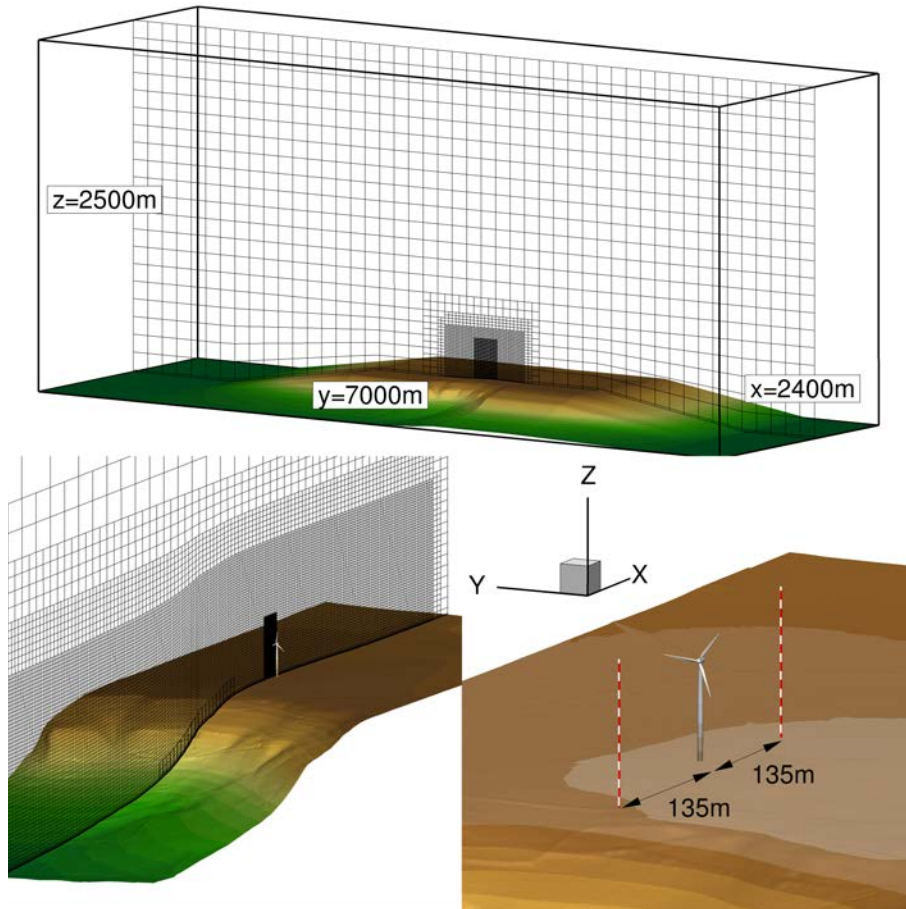
Figure 2. Background mesh and integration of the fully meshed wind turbine into the area; the mesh has been coarsened eightfold for presentation reasons. The upper plot shows the geometric dimensions of the computational domain and the resolution of the hanging grid nodes transverse to the flow direction. The lower left plot shows the resolution of the mesh in the inflow and in the wake of the turbine. A refinement grid around the turbine is also highlighted. The lower right plot shows a surface of the fully resolved turbine and the distances to the two met masts.

Figure 2 shows the geometric dimensions and spatial resolutions of the background mesh. Additionally, ~~the inte-~~
~~gration of~~ the fully resolved wind turbine ~~into~~ the background mesh ~~is depicted.~~ The ~~spatial~~ dimensions are 2500 m ×
7000 m × 2600 m in x, y and z directions. To ~~account for~~ any perturbations arising from the interaction between the topography and the lateral periodic boundary conditions, a large extension in the y-direction was introduced. This prevents from affecting the flow field in the centre of the domain through numerically induced pressure perturbations at the boundaries. The height of the domain was extracted in the z-direction up to 2500 m, since the atmospheric

80   boundary layer can extend ~~much~~ higher than 1000 m during summer months. To realise these dimensions with also
high resolutions in the relevant areas of the test site, the outer cells in y-, as well as in z-direction were coarsened
via hanging grid nodes. The relevant areas at the turbine and the met masts were discretised with a resolution of 1
m. In addition, a wide area was meshed with 2 m resolution to still be able to sufficiently resolve the flow physics
of large parts of the test site. In lateral and vertical direction, the structured mesh is then quickly coarsened to 4

85   m, then 8 m and finally to 16 m to save cells and consequently computational costs. As the lower-left plot shows,
the highly resolved (1 m) area extends through the entire domain with constant resolution in x-direction to avoid
numerical dissipation. The forest mesh is also illustrated within the grid in this section, which can be seen in the
bottom area at the escarpment. The application of thermal stability implies additional requirements for the mesh.
Unstable stratification requires a very wide and high domain because of the large height of the atmospheric bound-

90   ary layer and the large length scales, whereas the simulation of stable stratification requires a high resolution to
resolve the small eddies without losing much turbulent information through numerical dissipation. Considering these
requirements without increasing the computational costs ~~immeasurably~~ requires a careful choice of the background
mesh. The outer region of the mesh is coarsened by hanging grid nodes as described previously. The boundary layer
at the bottom surface is fully resolved with $y^+ \approx 1$.

95   To integrate the wind turbine into the field, as shown in the lower left plot, an additional mesh refinement in the
turbine's area was implemented with resolutions of 0.25 m.

The coordinate system is an inertial right-hand system that was arranged with $x = 0$ m at the turbine position. For
detailed wind turbine evaluations, the origin of the coordinate system was shifted to the hub position (x_{R0}, y_{R0}, z_{R0}),
which simplifies the interpretation of the results for these studies.

2.2   Numerical Setup

The compressible and block-structured finite volume flow solver FLOWer was used for the simulations. FLOWer
was originally developed by the German Aerospace Center (DLR) (Kroll et al., 2000). Since then, the code has
been extended and improved at the authors' institute for highly resolved simulations of wind turbines. Regarding
the boundary conditions, at the inflow a FLOWer internal boundary condition was chosen that allows the inflow of

105 user-defined turbulence or turbulence extracted from simulations or measurements. At the ground a friction no-slip
wall with the setting of a wall temperature was used. The lateral boundary conditions were chosen to be periodic. A
far-field boundary condition with 0-order extrapolation was set at the top boundary and at the outlet. This allows
inflow and outflow across the boundaries and behaves robustly regarding pressure gradients, which is important in
turbulent flows and especially for thermal stratification. This boundary condition also suppresses possible reflections

110 of disturbances at the numerical boundaries, which can arise from the standard far-field condition due to introducing
default values at the edges.

Regarding the numerical methods, the atmospheric boundary layer is simulated with the second-order Jameson-
Schmidt-Turkel scheme (Jameson et al., 1981) until a height of approximately 10 m above-the-ground, because of

the high aspect ratios caused by small cells and the orography. The rest of the domain is realised with a fifth-order
weighted essentially non-oscillatory (WENO) scheme (Schäferlein et al., 2013). The ~~used~~ turbulence model is the
Shear-Stress-Transport (SST) model from Menter (1994). Bangga et al. (2017) obtained the most stable results for
FLOWer with this turbulence model in DDES wind turbine simulations, which fit measured data best, justifying
the selection. It is also the most used model in the wind energy and helicopter aerodynamics working groups at the
authors' institute. An implicit dual-time stepping is applied for time integration with 100 inner iterations for each
time step. This setup is valid for all simulations of this study. The Courant-Friedrichs-Lewy (CFL) number in the
innermost domain was set to 0.4 for the simulations without wind turbine. For the sheared velocity profile, the hub
height was used as a reference position to determine the CFL number. After integrating the wind turbine into the
domain, the time step was reduced to adapt it to a rotor azimuth movement of 2°, which was needed for detailed
aerodynamic evaluations of the turbine. This resulted in a CFL number of 0.2. In order to achieve high accuracy of
the results, all studies in this paper were conducted with DDES simulations. Using this method, a shielding function
prevents the attached boundary layer from switching into the LES mode and generating grid-induced separation.
The area of the LES region and the region modelled with URANS were examined in a preliminary study. For this
purpose, the resolved areas of turbulence kinetic energy k_{res} were divided by the total TKE ($k_{tot}=k_{res}+k_{mod}$) for
each cell in the whole domain. Thus, the study revealed that cells of the lowest approximately 0.5 m above-the-
ground are modelled. The entire rest of the background mesh is simulated by LES. This preliminary study is valid
for all simulations shown in this paper.

2.3 Setup for the Comparisons with Measurements

The lower right plot of Fig. 2 shows the surface structures of the fully meshed wind turbine integrated into the
background mesh with the chimera technique (Benek et al., 1986). For the mesh of the rigid turbine, reference is
made to Guma et al. (2018) and Guma et al. (2020). As for the ground of the terrain, the no-slip wall boundary
conditions were introduced for the surfaces of the turbine. The two met masts of the test field have also been visualised
in this plot to reveal a spatial impression of the test field. The first one served as a validation and comparison basis
for this work. The wind turbine is about 135 m downstream of the first and about 135 m upstream of the second met
mast as can be seen in Fig. 1 and 2. The two wind turbines and the other two met masts are still under construction
and can therefore not serve as validation in this work. With the numerical simulations of the wind turbine, however,
far-reaching insights can already be gained through this study.

Table 1 reveals the met mast equipment used for this work as a validation basis. The met masts serve for com-
parisons with numerical results and to extract turbulence characteristics to generate synthetic turbulence at the
inflow. Cup anemometers, ultrasonic anemometers, and thermometers are primarily used for these studies. Both met
masts are equipped equivalently and have been installed downstream of each other in the mean flow direction. The
met masts and the wind turbine are located directly downstream of each other with negligible lateral offset. The

Table 1. Relevant equipment of the met masts

Measuring equipment	Height of the sensors [m]
Cup anemometers	10, 45, 59, 72, 89, 100
Ultrasonic anemometers	25, 50, 75, 100
Thermometers	3, 23, 45, 72, 96

orographic conditions on the plateau are very flat with only small height differences between the met masts and the wind turbine.

2.4 Forest Setup

150   As seen in Fig. 1, large parts of the test site, especially the escarpment, are covered by a dense forest. To be able to model vegetation in the simulation, adaptations in the FLOWer code are required, which were implemented in previous works (Letzgus et al., 2018). The implementation is based on the model of Shaw and Schumann (1992) for the implementation of leaf area densities above the height.

$$\boldsymbol{F_F} = \rho \cdot c_d \cdot a(z) \cdot |u| \tilde{u}_i \tag{1}$$

155   For this purpose, as described by equation (1), a force term was added to the momentum equations to apply forest modelling. The term is added to the right-hand side of the momentum equations according to equation (2). Besides the local velocities of the respective spatial direction, the force term also contains an empirical drag coefficient c_d, which is usually given as 0.15 in the literature, and the height-dependent leaf area density $a(z)$ (LAD). With an appropriate choice from measured or literature data, this parameter can model the drag that the vegetation exerts

160   on the flow field.

For the implementation of the forest, an additional grid structure is embedded into the background grid using the chimera technique in analogy to Letzgus et al. (2018) and Letzgus et al. (2020). In this way, the forest can be accurately defined numerically as a porous medium. Additionally, not only homogeneous forests with constant values of LAI and $a(z)$ can be modelled, as is typical in the literature, but variable leaf area densities and tree heights

165   can be modelled in each spatial direction. This strongly increases the accuracy of the replication of the forest shape in the simulations. It is implemented by adding a force term to each cell of the forest structure depending on the foliage density and tree height. Variable leaf area densities can thus be realised in any spatial direction.

The leaf area densities of two exemplary vegetations and the implementation of forests into the CFD domain are illustrated in Fig. 3. Since the leaf area densities of deciduous forests and coniferous forests are different, the upper

170   plot shows two curves for different vegetations. The curve with LAI = 2 shows a typical LAD profile of a coniferous forest above the height. The curve indicates small LAD values that change only slightly over the height because of the relatively uniform cover. A completely different profile is shown by the LAI = 5 curve, which represents a
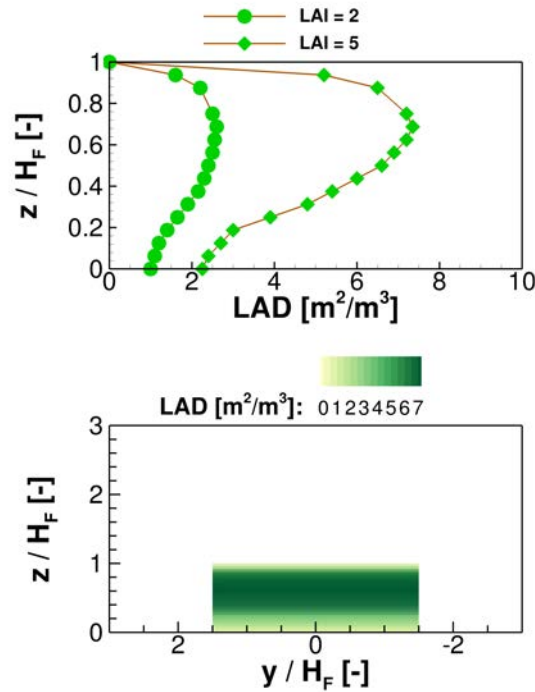
Figure 3. LAD of forests and their modelling in CFD

deciduous forest in summer. There, extremely large foliage densities are visible near the tree canopy, offering much greater drag to the wind than near the ground. The lower plot in Fig. 3 represents the height-dependent LAD for

175   a simple homogeneous forest with equal tree heights and equal foliage densities in the lateral direction. The shown LAD values are in analogy to the LAI = 5 curve from the upper plot. This represents the simplest generic case with laterally constant LAI values (LAI=5) and tree heights. The vegetation model is applied to the forest mesh structure. Maximum leaf area densities are found in the upper third of the vegetation height near the tree canopy. Accordingly, the maximum drag to the wind field is expected in this area, which is valid for most vegetation types.

180   However, this illustrates only a very simple academic case. For example, if a mixed forest is applied, the flow field will differ from a coniferous forest or a purely deciduous forest. Therefore, the vegetation species, the season, and the topology are also very important for forest modelling. On top of that, the height of the trees, the foliage densities and the distances between the trees are important for decent modelling. Thus, many factors must be considered when simulating forests. The explained approach tries to parametrise each part of the forest as accurately as possible

185   that the results of the highly resolved simulations achieve the desired quality.

Therefore, the model is adapted in a way that measured tree heights and realistic foliage densities are locally considered. Varying of the local foliage density according to the season and the species is captured, too. The detailed

dimensions of the forest in the test site are explained in the results section and the LAI values are listed separately for each simulation.

190   ## 2.5   Inflow Setup

The turbulence inflow data were generated with the Mann model (Mann, 1994), (Mann, 1998). The model is used by specifying the dissipation factor $\alpha\epsilon^{2/3}$, the turbulence intensity Ti, the stretching factor Γ of the turbulence gusts, and the largest length scales L that occur. This input is used to generate a turbulence box, which is applied in this work to simulate the evaluation of the turbulent atmospheric boundary layer. In order to implement this box,

195   the turbulent fluctuations are modelled by performing an inverse Fourier Transformation using the Mann model Spectrum and the Gaussian random complex variable. A velocity profile is specified at the inlet of the domain. After a distance of a few length scales downstream, the fluctuations generated by the Mann-box are fed in via force terms (Troldborg et al., 2014). After the propagation length of 4-5 further length scales the analytical spectrum has adapted to the real flow field with FLOWer (Müller et al., 2020), (Letzgus et al., 2020).

200   For the generic case studies of this work, the parameters of the Mann model were selected from experience and literature values. For the subsequent real case conditions, experimental data from measurements were used to extract the turbulence parameters. The required turbulent quantities were extracted from the measurement data of the first met mast. The turbulence intensity and the length scales were extracted and, depending on the thermal stability, the dissipation factor $\alpha\epsilon^{2/3}$ and the stretch factor Γ were adjusted.

205   ## 2.6   Thermal Stability Setup

The Mann model in its original form is only valid for neutral conditions. However, as described by Chougule et al. (2016), adjustments can be made to capture turbulence under atmospheric stratification. For thermal stability, the parameters of the Mann model must be adjusted, as different thermal conditions also affect the length scale L, turbulence intensity Ti, dissipation rates $\alpha\epsilon^{2/3}$ and the anisotropy Γ. As the mechanically and thermally generated

210   dissipation rates of $\alpha\epsilon^{2/3}$ are of similar magnitudes for neutral and unstable stratification, the thermal effect of stable stratification and suppressed turbulent mixing results in a reduction of this factor and thus in lower dissipation. The fit of the $\alpha\epsilon^{2/3}$ parameters for different stratifications is reported by Chougule et al. (2016) in his study of the Rapid Distortion Theory (RDT) for buoyancy influences under stratified conditions. The stretching parameter Γ also varies for different stabilities, since the anisotropy is also much smaller for unstably stratified turbulence than for stably

215   stratified turbulence.

However, thermal stratification not only changes the spatial properties of turbulence. To account for atmospheric stratification, the FLOWer code was extended to allow profiles of potential temperature to be propagated through the field to represent different conditions of stability. Using this approach, a wall temperature is specified, and a potential temperature profile is fed into the flow domain at the inflow plane by adjusting the energy equations. The

220   potential temperature field is propagated through the domain together with the atmospheric turbulence. This means

that the field is initialised with a default value of the potential temperature and afterwards the temperature field is propagated through the domain. Therefore, depending on the thermal stability, the respective heat flux is simulated, which results in buoyancy.
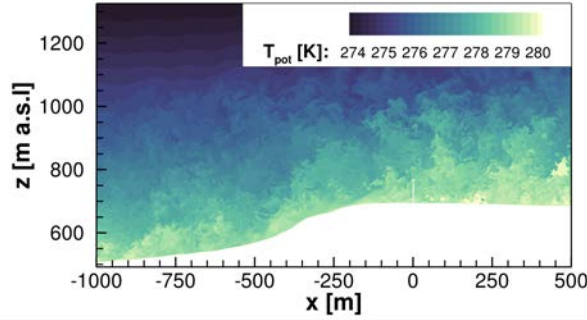
Figure 4. Vertical plane illustrating the development of potential temperature for unstable conditions; wind turbine at x=0 m

Figure 4 shows an exemplary contour of the potential temperature in a vertical plane through the 3D field at an
225 arbitrary time. It illustrates the profile of the potential temperature in the presence of unstable stratification in complex terrain with the wind turbine at x=0 m. The plot is intended to serve as an example of the newly implemented feature to consider the impact of potential temperature.

To implement an approach to consider atmospheric stratification, the momentum equations must include the buoyancy force, which depends on the change in potential temperature over height and acts positively directed upward for
230 unstable stratification and negatively directed downward for unstable stratification. For this purpose, the momentum equations are adapted analogously to Churchfield et al. (2014) in equation (2).

2.7   Governing Equations

The resulting momentum equations are represented by equation (2). On the right-hand side of the equation, besides the external force term of the forest model F_F, the buoyancy force is implied. This convective force results from
235 density differences of air parcels ρ_k with their surroundings ρ_0. The reason for these density differences are gradients of the potential temperature.

$$
\begin{aligned}
&\frac{\partial\left[\langle\rho\rangle\cdot\tilde{u}_i\right]}{\partial t} + \frac{\partial\left[\langle\rho\rangle\cdot\tilde{u}_i\tilde{u}_j\right]}{\partial x_j} + \frac{\partial\langle p\rangle}{\partial x_i} \\
&= -\frac{\partial\left[\tilde{\tau}_{ij} - \langle\rho\rangle\cdot\widetilde{u_i''u_j''}\right]}{\partial x_j} - g_3 z \frac{\partial}{\partial x_i}\left(\frac{\rho_k}{\rho_0}\right) + F_F
\end{aligned}
\tag{2}
$$

3   Results - Part 1 Case Study of General Effects

An analysis of the different effects that have a significant impact on the flow field is presented in the first part of

240   the results. Initially, the focus is on the forested escarpment of the test site. Subsequently, the impact of thermal stratification on the test site is shown, and finally, the wind turbine is ~~integrated~~ into the domain.

Through this method, several parameters that determine the flow field at the test site can be examined separately. In the second part of the results, all effects are combined and applied to a real case study.

3.1   Effects of the Forested Escarpment on the Flow Field

245   In the following, ~~it will be~~ investigated ~~to what~~ extent the flow field is affected by the forest at the wind energy test site. To simulate forests in a highly resolved approach, forest heights and foliage densities must be analysed to model the trees accurately. For this purpose, Digital Elevation Models (DEM) and Digital Surface Models (DSM) with 1 m resolution provided by the State Office for Geoinformation and Land Development in Stuttgart (LGL) were used to determine the heights of the vegetation on the test site. In contrast to the DEM, the DSM also includes

250   the topographic aspects of buildings and vegetation in addition to the orography of the terrain. Thus, the heights of trees and buildings are determined by subtracting the DEM and the DSM model heights. The result is shown in detail in Fig. 5.
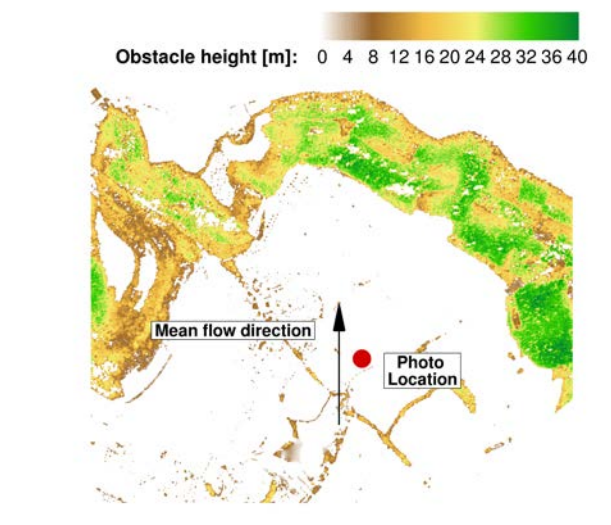
Figure 5. Vegetation and building heights on the test site. The info is used for detailed modelling of the tree heights

The part of the Albtrauf near Donzdorf is characterised by a mixed forest consisting mostly of beech and spruce, as typically the most parts of the forests of the Swabian Alb (ForstBW, 2021). There are almost no clearings on

255   the entire escarpment. In general, trees are 20 to 35 meters tall. Regarding the mixed forest, seasonal variations

in foliage cover occur that affect the LAI and consequently the flow field downstream of the forested escarpment. Figure 6 shows a photo of the forested escarpment taken on 26 March 2021 near the position of the numerical inflow

Figure 6. Photo at the position of the inflow plane with a view in flow direction onto the forested escarpment of the test field. Above the forest, the tops of the met masts are visible

plane. The tops of the two met masts are visible in the background on the plateau. For visualisation reasons, the representation of the met masts has been highlighted with red lines. A close look at the photo illustrates how sparsely

260 covered the forest was in the early part of the year. However, the Albtrauf is also characterised by spruce stands, so the winter LAI is approximately 2 m² m⁻² since the trees are typically close together at the escarpment. In contrast, the mixed forest in the summer months is modelled with a mean LAI of 4.5 m² m⁻². The forest heights were modelled analogously to Fig. 5 in the simulations. The used LAI values are specified separately for each simulation.

Emeis (2013) described how the forest cover affects the flow field in flat terrain. A forested escarpment ~~even~~ increases

265 the influence on the local flow field. Thus, the effects of the forested escarpment on the flow field are analysed in detail.
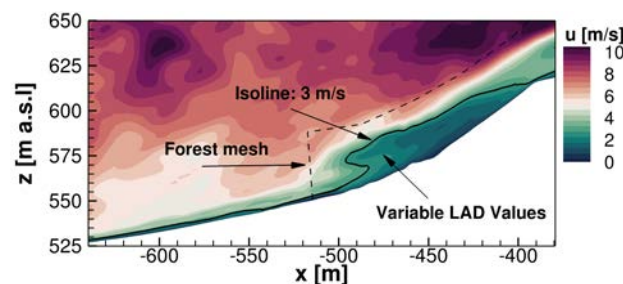
Figure 7. Detailed flow field of the forest in a vertical plane

A detailed illustration of the simulation of the forested escarpment is given by Fig. 7. In a vertical plane that also crosses the wind turbine position further downstream, the flow situation at the beginning of the forested escarpment is visible. The forest was modelled with an LAI value of 4.5 and the flow field shows ambient turbulence with an intensity of 10% with a mean speed of 8 m s^{-1} at hub height in the valley with an initial length scale of 40 m. In the simulation, the corresponding Hellmann exponent was chosen to be $\alpha = 0.17$. The influence of the forest is evident. The impact in the flow field is highlighted by an isoline representing a velocity of $u = 3$ m s^{-1}. This line indicates how the leaf area density over height was modelled at this position. The forest mesh is sketched with a dashed line to highlight the extent of the forest within the terrain.
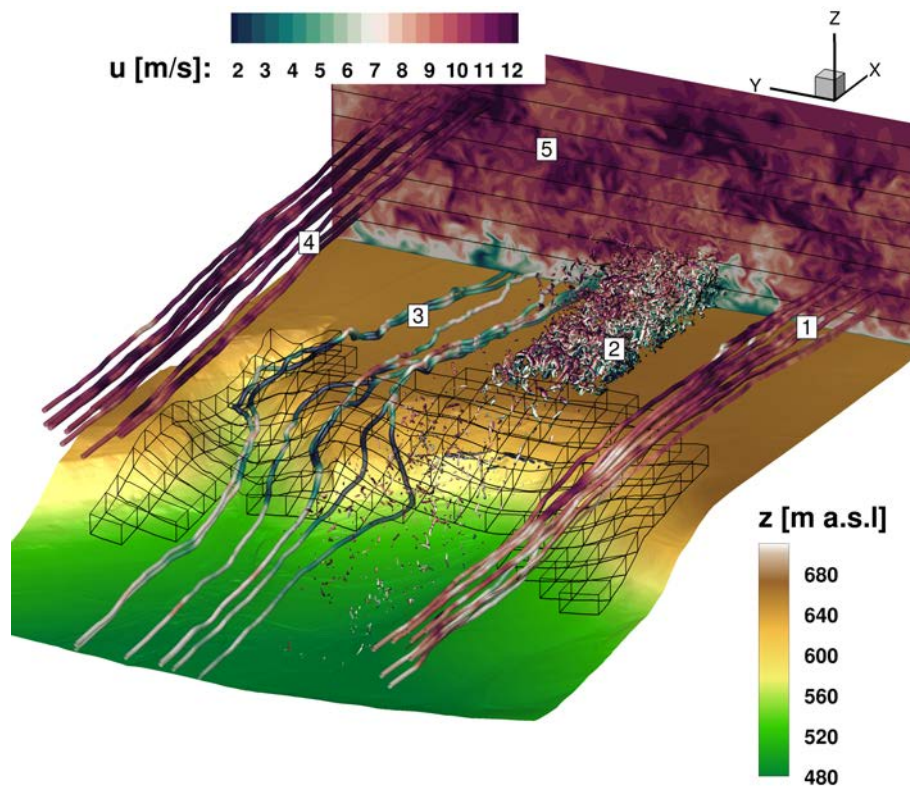
Figure 8. Flow situation in the test field shown in detail with highlighting of five characteristic flow areas

Figure 8 depicts the flow field of the complete test site for an arbitrary moment. The simulation results show the same inflow parameters as described before. The forested area is marked by black blocks and different flow regions have been given numbers to analyse the individual flow conditions separately. The respective flow phenomena have been intentionally drawn only in certain regions for clarity, since they occur across the entire width of the domain. Area $\boxed{1}$ depicts streamlines coloured analogously to the respective horizontal wind speed. This area shows the lower part of the flow field just above the forest canopy. The colour change from red-white to dark red clearly highlights

the typical effect of accelerating flows over hills or ridges. This area also represents the flow region that mainly crosses the rotor plane. Downstream of the escarpment at hub height, the wind reaches a speed of 11 m s^{-1}. This means that the speed increase at the hub height due to the escarpment is 3 m s^{-1}. Area $\boxed{2}$ illustrates turbulent structures using the λ_2 vortex criterion. This emphasises the strong mixing of turbulence structures in the wake of the forest. There, considerable low axial velocities and high standard deviations occur. The turbulence is further amplified by the superposition of the turbulent forest wake with the accelerated flow from area $\boxed{1}$. A flow region results that comprises high turbulence intensities and large velocity differences. Flow region $\boxed{3}$ visualises streamlines in the near-ground region crossing the forest. The blue colouration of the streamlines illustrates the reduction of wind speed due to the forest. Besides, because of the orography and the different leaf area densities above the height and width of the heterogeneous modelled forest, these streamlines are strongly curved and exhibit locally large changes in direction. The shear layer between the flow regions $\boxed{1}$ and $\boxed{3}$, which exhibits large velocity differences, amplifies the generation of turbulent fluctuations. This is visible for region $\boxed{2}$. The same effect has already been analysed and explained by Dupont et al. (2008). Flow region $\boxed{4}$ shows the upper flow field a few hundred metres above-the-ground. There the streamlines are no longer inclined and the influence of the orography is negligibly small. Therefore, the flow does not accelerate when streaming over the escarpment. The small curvatures of the streamlines and velocity changes are only caused by atmospheric turbulence. Area $\boxed{5}$ depicts a plane on the flat plateau of the test field, which is perpendicular to the flow direction and captures the horizontal wind speeds. This provides a view of the turbulent flow field with all the effects described previously. From Fig. 8 it can therefore be shown that in complex terrain many different orographic and topographic effects influence the flow field and thus the inflow of wind turbines. Especially the wake of a forested escarpment, with trees reaching the plateau on top of a slope, influences the flow field to a great extent.

The above-mentioned influences are based on simulations of summer months with an average LAI of 4.5. A variation of the leaf area densities and a comparison of the influences on the test field will be investigated in the following by using the same inflow conditions.
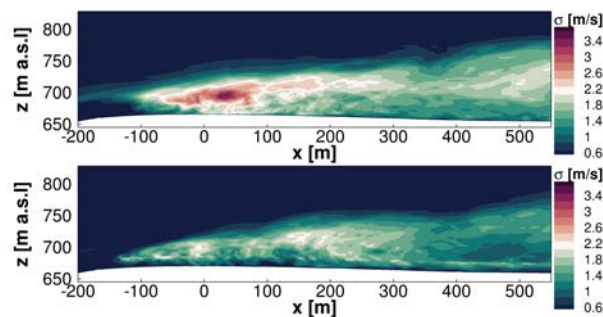
Figure 9. Standard deviation of horizontal velocity in forest wake for different Leaf Area Indices. Upper plot: LAI = 4.5 for foliage cover in summer. Lower plot: LAI = 2 for foliage cover in winter

305   The standard deviations of the horizontal velocity in the wake of the forest on the flat plateau of the test site with the corresponding LAI values for summer and winter months are shown in Fig. 9. For the evaluation, the respective flow fields were averaged over four minutes. The upper plot demonstrates the standard deviation in summer months with an LAI of 4.5 and the lower plot for winter months with an LAI value of approximately 2. Using these values was valid because of the spruce stands on the escarpment. Lower values than 2 would be typical for pure deciduous

310   forests in the winter months.

    At first glance, significant differences of the standard deviation σ become apparent. The higher leaf area densities in the summer months result in stronger amplification of turbulence and consequently to significantly larger standard deviations than in winter months. Especially in the turbine's area at x=0 m, the fluctuations are significantly lower for the sparsely covered forest. It is worth mentioning that the propagation of the standard deviation behaves

315   analogously for both forest covers. This means the turbulence is more amplified by the denser forest, but the forest wake expands to similar ranges in height and width (for the same wind conditions) in the summer and winter months. Consequently, the forest effect is measurable at similar heights for different foliage densities. However, the atmospheric boundary layer in the forest wake will recover more quickly further downstream for the sparsely covered forest due to lower turbulence intensities.

320 **3.2   Effects of Thermal Stability on the Flow Field**

    Next, the influence of thermal stratification on the flow field is analysed. Three simulations with the same inflow conditions and turbulence characteristics are compared. However, the buoyancy varies because of different thermal stratification conditions. As described in Sect. 2.6, the inflow conditions and turbulence characteristics differ significantly for stable and unstable conditions. The following results, however, aim exclusively to explain how thermal

325 effects can affect flow fields. The turbulence intensity for each case was set to 8%. The results were assessed at the same time or averaged over a period of four minutes.
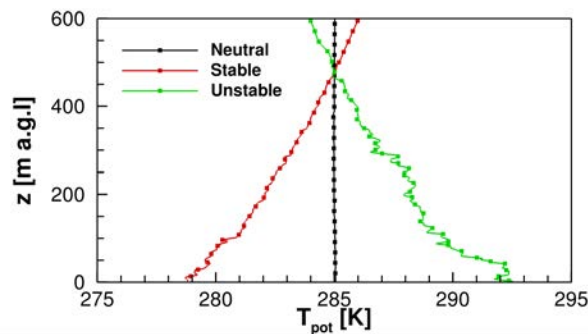
Figure 10. Profiles of the potential temperature of the three atmospheric stratification conditions extracted from their respective flow fields

Profiles of potential temperature extracted at position x = -750 m are shown in Fig. 10. These three curves illustrate simulations of neutral, stable, and unstable stratification, respectively. The gradients of the potential temperature reveal that these are quite strong cases of atmospheric stratification. Although these are strong conditions, they are

330   likely to occur in nature and are intended to clarify the general effects of buoyancy in this study. The depicted lines belong to particular stratification conditions, which are also illustrated in Fig. 11.
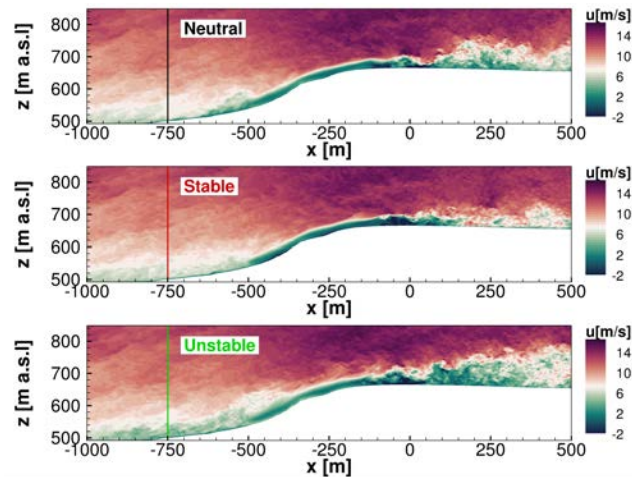
Figure 11. Snapshots of extracted vertical slices of the flow field under different stratification conditions

In Fig. 11, three snapshots of the simulation results are illustrated simultaneously in different stability conditions. Based on the gradient of potential temperature from Fig. 10, the buoyancy is calculated. All three cases are investigated using the same inflow conditions. This is not the case in nature, because thermal stability also affects the

335   properties of turbulence, such as its intensity, length scale, and dissipation. The study, however, aims to assess the effects of buoyancy in general.

The flow field in neutral conditions is shown in the upper plot. Results for stable and unstable conditions are shown analogously in the middle and lower illustrations. It can be observed that atmospheric turbulence changes due to buoyancy in the flow region close to the inflow between x = -1000 m and x = -600 m. The forest wake even amplifies

340   buoyancy effects. In the wake of the forest, the influences of buoyancy become evident. Using the flow field for neutral conditions as a reference case, it is noticeable that stable stratification suppresses the mixing of the forest wake with the ambient turbulence. Consequently, the wake exhibits smaller fluctuations and does not extend to high altitudes. Unstable stratification has the opposite effect. Thus, the wake and ambient turbulence are mixed and propagated to larger heights, resulting in higher turbulence intensities. Ultimately, unstable conditions influence the test site and

345   the wind turbine inflow more than other conditions, which will be emphasised hereinafter.

The standard deviations σ of the horizontal velocity are displayed in an enlarged graph of the forest wake in Fig. 12. In a four-minute time window, standard deviations were evaluated. The upper plot shows the flow field for
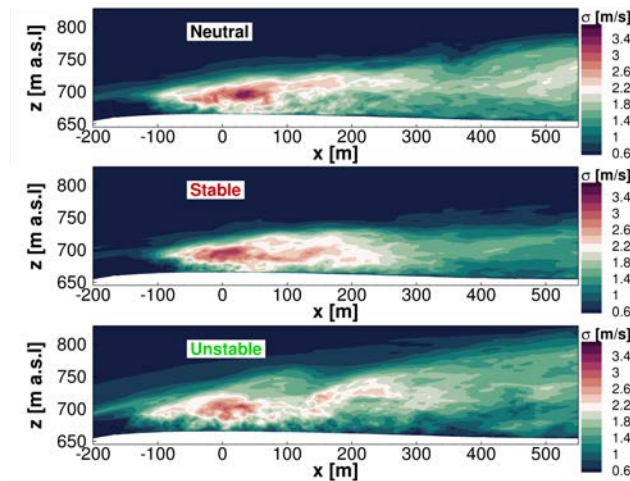
Figure 12. Standard deviation of horizontal velocity in the forest wake for different stratification conditions

neutral stratification, the middle plot for stable stratification, and the lower plot for unstable stratification. Again,
neutral stratification is chosen as a reference case. Further downstream, the standard deviation decreases, indicating

350 a reduction in turbulent fluctuations, although the wake extends to higher altitudes. For stable stratification, the
standard deviations in the forest wake decrease compared to neutral conditions. This suppresses turbulence, causing
the σ values to decrease significantly. On top of that, the wake does not extend to higher altitudes. A similar result
was obtained by Desmond et al. (2017) both numerically and in wind tunnel measurements. The opposite effect is
again evident in the lower plot for unstable stratification. The standard deviation decreases with increasing distance

355 to the forest, but the turbulence in the forest wake spreads in much higher altitudes than for other conditions.

Figure 13 compares distributions of flow variables for stable and unstable stratification at the turbine position
(x=0 m) versus altitude. The dimensions of the rotor plane are highlighted by the dashed lines and the hub height
by the solid line. The upper plot shows the mean velocity profiles. Stable stratification causes increased velocities
at smaller altitudes, in contrast to unstable conditions. The reason for this is buoyancy-induced higher velocities in

360 stable conditions versus unstable conditions. Air masses from higher altitudes, which generally show higher velocities
caused by the shear of the atmospheric boundary layer, move vertically downwards into lower areas due to buoyancy.
For unstable conditions, the forest wake also has a stronger effect on the velocity field as shown in Fig. 12. The
study of Keck et al. (2013) confirms these results. According to their research, if the wind flows over and around hills
in stable conditions, there will be higher accelerations and consequently higher velocities. The lower plot shows the

365 comparison of standard deviations versus altitude. Compared to the profile for stable conditions, there is a significant
increase in mixing of the air for unstable stratification. Due to the amplified turbulent mixing, the standard deviation
for the entire height is higher than for stable stratification. Especially near the ground and in the forest wake this
can be quantified. Besides the lower wind speed, the increased turbulence also affects the wind turbine rotor plane
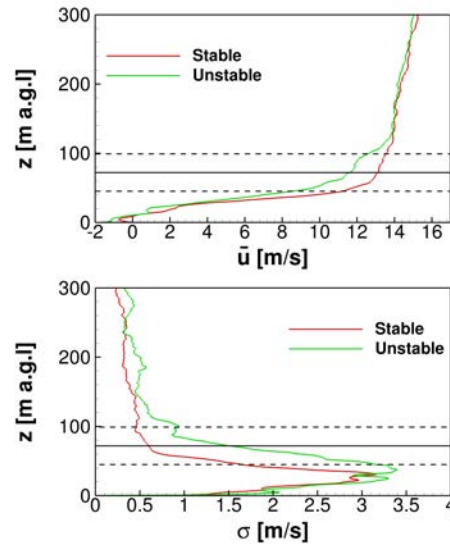
Figure 13. Comparison of flow variables at the turbine position versus altitude for stable and unstable stratification. The rotor plane is also marked in both plots

more for unstable stratification than for stable stratification. For stable stratification, the influence of the forest
370 wake at the rotor plane is small, and only noticeable for turbulent quantities, whereas under unstable conditions the
turbine's inflow is significantly affected.

Transverse planes at the wind turbine position will further emphasise these effects as can be seen in Fig. 14.

Figure 14 depicts the flow field at the turbine position for neutral, stable, and unstable stratifications. It visualises
again the standard deviation of the horizontal mean flow field. Especially the influence of the vegetation on the flow
375 field at different stability conditions will be further investigated, based on the findings in Fig. 13. Besides the plane at
the turbine location, the forested areas are also shown. In the contour slice, the rotor area is sketched with a yellow
circle. This is supposed to show how the wind turbine is affected by the flow field of the forest wake for different
stabilities. The buoyancy force determines the mean flow field. As compared with other thermal conditions, fluid
mixing in the forest wake spreads over the entire width to higher altitudes for unstable stratification. Thus, the forest
380 wake also crosses the rotor plane. This dominant effect is visible in the lower plot. For neutral stratification, vortex
structures detaching from the forest only sporadically cross the lower half of the rotor. For stable stratification, there
are only scattered turbulent structures influencing the rotor. On average, for stable conditions, most of the rotor
remains unharmed by the forest wake.

3.3 Forest Effects on the Wind Turbine

385 In the following, interaction of the forest wake and the wind turbine is investigated for neutrally stratified conditions.
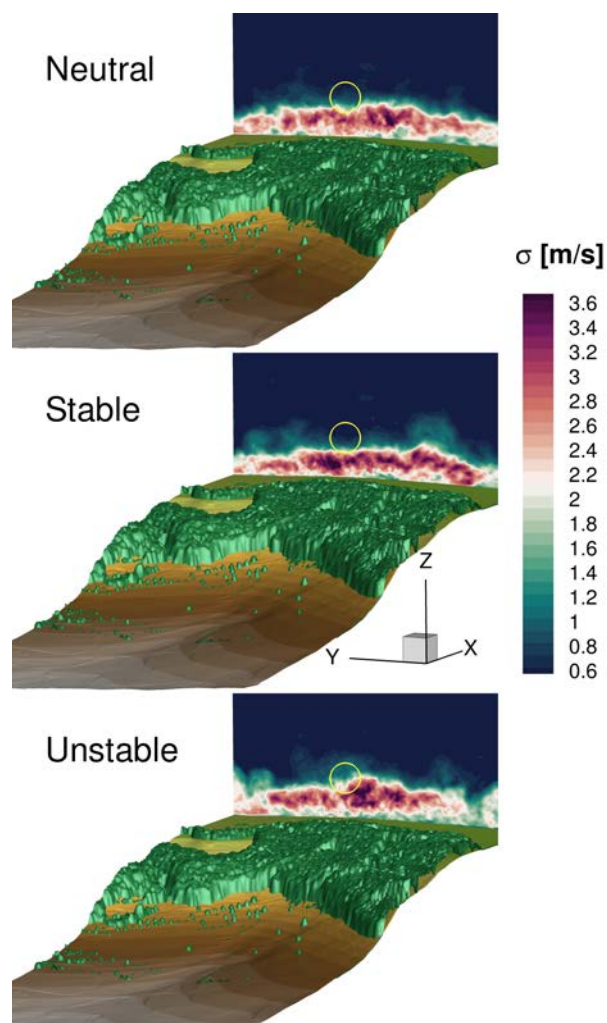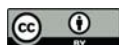
Figure 14. Standard deviation of the horizontal velocity at the wind turbine position. The rotor position is outlined by the yellow circle

Figure 15 shows an unsteady flow situation in which the forest wake and atmospheric turbulence interact strongly with the wind turbine and its wake. The wind turbine was integrated into the computational domain of the same simulation as in Fig. 8. The initialised fully meshed wind turbine was subsequently simulated over a period of a few rotor revolutions in order to eliminate numerical disturbances that arise when the turbine is integrated into the numerical domain. After further 25 revolutions, this plot was extracted. A vertically oriented plane of the local velocity was extracted to illustrate the flow field at the topography. Additionally, λ_2 structures of turbulence are shown to indicate the strong interaction of the forest wake, the ambient turbulence, and the turbine. After the propagation of only a few rotor revolutions, the blade tip vortices break down into smaller turbulent structures.
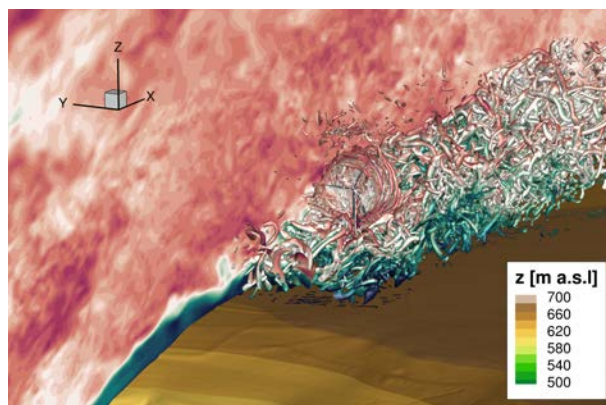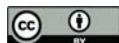
Figure 15. Snapshot of the interaction of the wind turbine with the forest wake and the ambient turbulence

Further downstream, there is a turbulent low speed area, where the turbine wake and the forest wake can no longer be distinguished. More detailed analyses of this effect are presented below. In the following section, two different
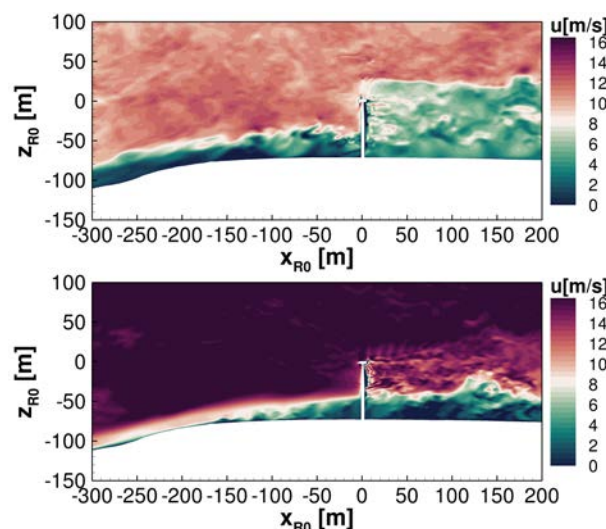
Figure 16. Vertical planes of the interaction of forest wakes, ambient turbulence and wind turbines for two different flow cases

395   flow and vegetation conditions will be analysed to develop a physical understanding of the topography-forest-turbine interaction. Figure 16 shows the interaction of the forest wake and the wind turbine. In the upper plot, the same flow situation as described before is analysed, which reaches rated turbine conditions of 11 m s^{-1} at hub height with a turbulence intensity of 10%. Again, this study is intended to show a summer situation with relatively high wind

400   speeds. Here, the forest is completely leafy and accordingly has an LAI of about 4.5. Occasionally, vortex structures

of the forest wake cross the rotor plane, which leads to large velocity fluctuations that may influence the rotor loads and the turbine performance negatively. In the upper plot, the dense forest causes vortex shedding at the canopy, which can randomly affect the inflow onto the wind turbine. A large area of reduced wind speeds is displayed from the upper blade tip to the ground downstream of the turbine. The forest wake quickly mixes with the turbine wake, leaving a large common wake area. In the lower plot, a comparable vertical plane is shown at higher wind speeds. This is a simulated real flow scenario from 31 March 2019 at 11 p.m. at the test site with average wind speeds of 16.5 m s^{-1} at hub height. A turbulence intensity of 9% and a length scale of 35 m was measured at the met mast, which was adjusted to the flow situation in the valley and then used as inflow data for the FLOWer simulations. As the forest is not completely leafy in spring it was modelled with an averaged LAI of 2.8. Because of the high wind speeds, the rotor blades are provided with larger pitch angles, which is the reason why the velocities of the wake are not reduced as much by the turbine as in the plot above. By contrast, the inflow of the wind turbine is less affected by the sparsely covered forest, but downstream of the wind turbine a strong interaction between the forest wake and the turbine wake is readily apparent. Caused by the higher velocity differences of turbine wake and forest wake, they do not mix to the same extent as in the upper plot of Fig. 16. However, the small velocities in the forest wake affect a deflection of the turbine wake. There is a noticeable vertical wake deflection at x=130 m, which strongly influences the turbine wake propagation. As a result, the forest wake and the turbine wake do not mix as strongly as they do in the upper plot, but the speed differences of the turbulent structures result in significant deflections. Thus, neutral stratification and different leaf area densities result in large forest-turbine interactions, which have a significant impact on inflow and wake.

3.4 Thermal Stability Effects on the Wind Turbine

In the following, influences of different stratification conditions with consideration of the wind turbine are compared. For this study, the influence of vegetation will be neglected to capture the effects of buoyancy on the inflow and wake of the wind turbine separately. For this purpose, the inflow conditions from Fig. 11 and 12 were again used. With ~~integrating~~ the turbine into the flow field, the forest was removed as just described, to investigate only the influence of buoyancy and ambient turbulence on the wind turbine in complex terrain.

Standard deviation σ ($\sigma = \sigma_u + \sigma_v + \sigma_w$) of planes perpendicular to the flow direction several rotor diameters (2D, 4D and 6D) downstream of the wind turbine are illustrated in Fig. 17 and 18. Figure 17 represents the wake cross sections for the simulations under stable conditions and Fig. 18 for unstable stratification. Through the standard deviation σ, the shape of the wake and the mixing with the ambient turbulence are explained. It becomes apparent that further downstream the fluctuations of the wake are considerably larger for unstable stratification than for stable conditions. Comparing the standard deviation σ in Fig. 17 with Fig. 18, it is recognisable that already 2D downstream of the turbine the plots look entirely different. In this region primarily the blade tip vortices cause these high values of the standard deviation. For unstable stratification, the vortices spread out into significantly wider areas, whereas for stable stratification the wake keeps its circular shape longer. Further downstream, it can
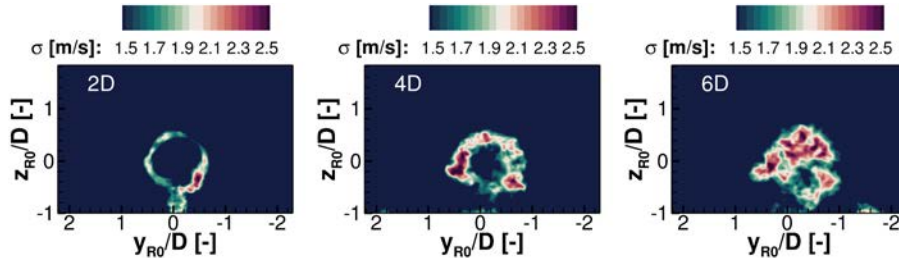
Figure 17. Standard deviations of the wake for stable stratification in transverse planes several rotor diameters (2D, 4D and 6D) downstream of the wind turbine
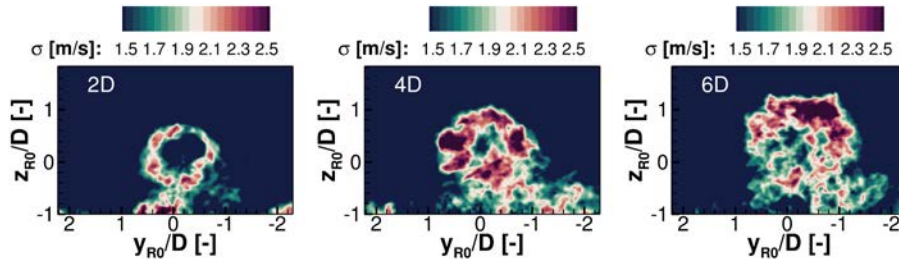
Figure 18. Standard deviations of the wake for unstable stratification in transverse planes several rotor diameters (2D, 4D and 6D) downstream of the wind turbine

435   be assumed that the wake decays for unstable conditions more quickly, due to vortex breakdown, as analysed by Troldborg et al. (2008). In stable stratification, the vortex decay will occur comparatively further downstream due to suppressed mixing, which is evident from the standard deviation at all planes.

4   Results - Part 2 Real Case Study: 10 March 2021

In the second part of the paper, the previously described effects on flow fields in complex terrain are investigated
440   combined for a case study based on real-life conditions. For this study, a five-minute time period of the measurement data from 10 March 2021 at 11:30 a.m. was extracted to generate inflow data in the valley. This was then propagated through the domain and compared to the experimental data. On the plateau, the flow direction is west-northwest, which corresponds with the predominant wind direction at this site. The atmosphere was slightly unstable stratified, and the forest was not leafy because of the springtime considered here. The turbulence and the velocity profile were
445   measured by the met mast. To obtain the velocity profile at the inflow plane, the measurement data were adjusted to the flow field in the valley. This resulted in a reference velocity $u_{ref} = 4.8$ m s^{-1} at the hub height $z_{ref} = 72$ m with an Hellmann exponent $\alpha = 0.2$ at the inflow plane. The synthetic turbulence for this purpose was generated with a turbulence intensity of Ti=15%. The used length scale was 42 m, which is consistent with findings of Peña et al.

(2010) and Sathe et al. (2013) for slightly unstable conditions at comparable wind speeds. The ~~stretching factor~~ Γ
450   was set to 3.9 and the dissipation factor $\alpha\epsilon^{2/3}$ was set to 0.03 for higher dissipation for unstable conditions. Because
of insignificant wind veer, the Coriolis force is ignored.
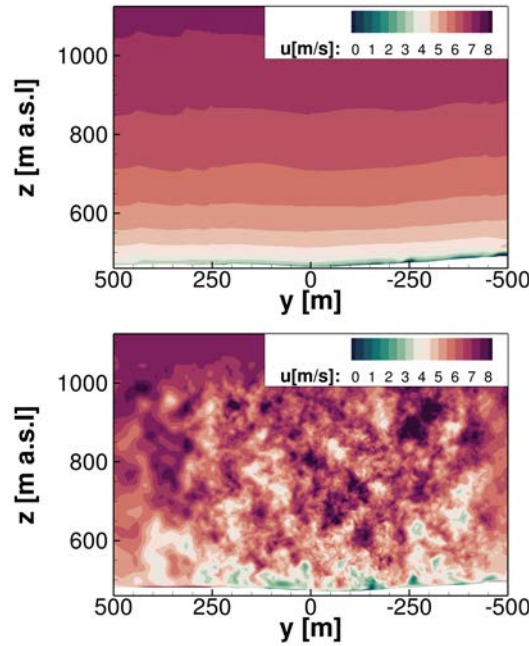
Figure 19. Generation of turbulence from the met mast data of 10 March 2021 and the resulting turbulent flow field at the
inflow

The generated unsteady inflow plane is shown in Fig. 19. The used velocity profile at the inflow is illustrated in the
upper plot. This above-the-ground extracted velocity profile is superimposed with the generated synthetic turbulence
by source terms. The resulting flow field is shown in the lower plot at a position two length scales downstream of
455   the inflow plane. This transient turbulent field is propagated through the domain. After one complete flow through
the whole domain, the evaluation, as well as the averaging of the simulation, was started in order to compare it with
the met mast data as shown by Fig. 20.

Figure 20 illustrates the comparison of simulated flow quantities compared with experimental data of the first
met mast. Both the measurements and the simulations show results, which are averaged over five minutes. The
460   mean velocity profile at the met mast position is depicted in the left plot. The forest wake with reduced velocities
near the ground causes the almost linear increase of the curve until 50 m a.g.l. In the upper part of the velocity
profile near the rotor plane and above, there is very little shear of the wind speed. The wind speed remains almost
constant over the height, which can be explained by the over-speed over the terrain in lower areas, whereas the
upper flow field is less influenced by the orography. This effect has also been illustrated by flow regions 1 and
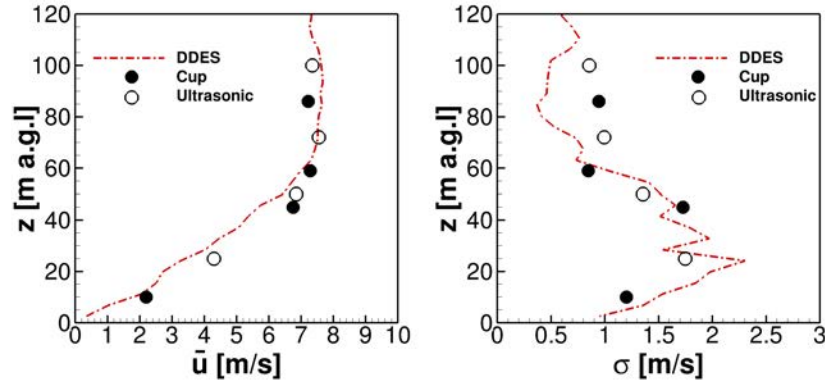
Figure 20. Averaged flow quantities of the simulations in comparison with measured mast data from 10 March 2021

465   4   in Fig. 8. Besides, the shear is suppressed by the convective conditions in this situation, because the buoyancy force drives air masses upwards. It is noticeable that the numerical results show a decent agreement compared to the measured data. The deviation of all measurement points to the simulated results remains in a range of ± 1 m s^{-1}. The graph of the standard deviation σ above the height is shown in the right plot. Up to 60 m above-the-ground, the standard deviation and consequently the turbulence is significantly increased, which is shown in both

470   the simulation and the measured data. The forest wake, which extends to higher altitudes because of the unstable conditions primarily causes this effect. A stronger mixing of the ambient turbulence and the forest wake is the result. In this region, the examined turbulence properties match well with the CFD simulations. At higher altitudes, there are deviations of the numerics and the measured data. This can probably be explained by the evaluation period in the simulations, whereby the synthetic turbulence generated stochastically via the Mann model did not exactly

475   match the real turbulence characteristics. These turbulent data were fed into the inflow plane in the valley more than 1000 m upstream of this evaluation position.

A plane through the rotor position is visualised in Fig. 21. In the upper plot, the flow field at an arbitrary moment in time is shown. The interaction of the turbine rotor, the ambient turbulence, and the turbulent wake of the forest are shown. The situation depicts the flow field 65 revolutions after the rotating turbine has been integrated into the

480   flow field. From the turbulent structures of the forest wake, which propagate heterogeneously and expand to different heights, it becomes evident that with increasing time, detaching vortex structures with low horizontal velocities cross the rotor plane. Investigating the lower plot, the turbulent inflow onto the turbine is characterised. The turbulent forest wake extends on average into heights of 45 m. The significantly increased turbulence intensity results from fluctuations at low mean velocities in the forest wake. If these structures flow through the rotor plane, the inflow

485   will be significantly affected. This influences the loads, the power, as well as the wake. Especially in the lower right rotor position, the high turbulence intensity caused by the forest wake are remarkable. The effect on the wake is explained in the following Fig. 22. The effects on power output and rotor loads follow afterwards.
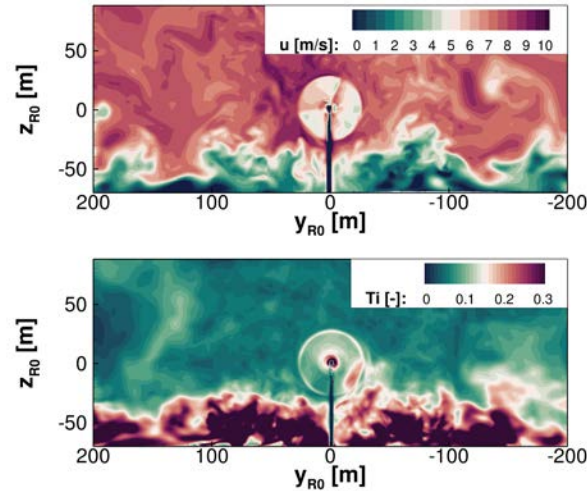
Figure 21. Flow situation at the wind turbine position for unstable conditions on 10 March 21. Upper plot: Instantaneous flow field. Lower plot: Turbulence intensity of the flow field

Figure 22 shows a vertical plane of the instantaneous flow field upstream and downstream of the wind turbine. Despite the lower foliage densities, the unstable conditions lead to significant mixing of the ambient flow with the forest wake, which also affects the inflow on the wind turbine. However, especially the effects on the wake are even stronger. Up to $x = 200$ m downstream of the turbine, the turbine wake is distinguishable from the forest wake. The propagation of the blade tip vortices with increased velocities is also visible in this area. Further downstream the wake structures of the forest and the wind turbine increasingly mix and are hardly distinguishable from each other. Considering a position that lies even further downstream, a decay of the turbulent wake is noticeable. Temporal averages show similar findings. The middle plot shows such an averaged flow solution over 60 seconds. The lower plot indicates the turbulence intensity evaluated over the same period. Starting at $x = 200$ m, the wake contour of the turbine mixes with the forest wake to an extent that results in a uniformly spreading wake structure, which rapidly decays. Also increasing fluctuations arise from the strong mixing of the wind turbine wake and the forest wake. The turbulence production near the ground at $x = -140$ m downstream of the last tree row is due to transient effects: A combination of temporal flow separations and also moments with high velocities at this position causes these unsteady variations of the wind.

Thus, the high turbulence intensities at these unstable conditions lead to strong fluctuations in the wake. This impact causes the wake to deform when mixing with the forest. The result is a breakdown of the wake further downstream.

The physical behaviour of the flow in the wake will be examined in more detail by looking at transverse planes in Fig. 23 and Fig. 24. The planes are extracted 2, 4, and 6 rotor diameters downstream of the turbine, respectively. Figure 23 shows the averaged axial induction factor a to analyse the mean wake propagation. Figure 24 examines the standard deviation σ, which is used to evaluate the decay of the wake with increasing distance. In a distance 2D
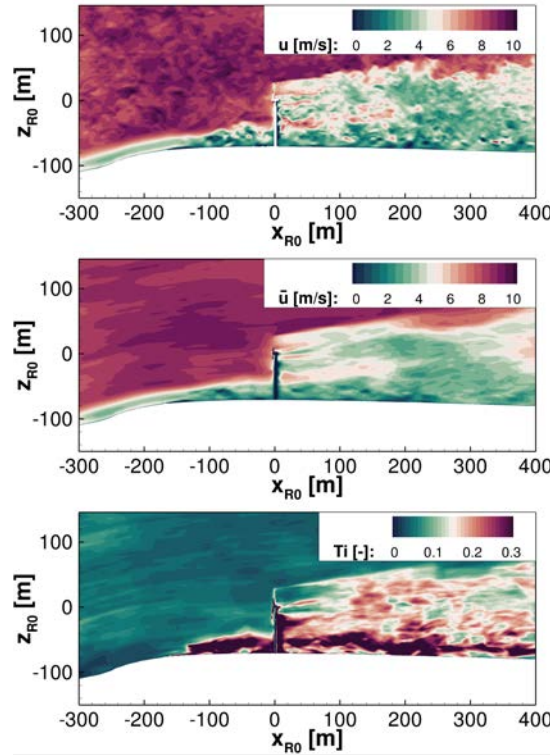
Figure 22. Flow field of a vertical plane crossing the wind turbine position during unstable conditions on 10 March 21. Upper plot: Instantaneous flow field. Middle plot: Averaged flow field. Lower plot: Turbulence intensity of the flow field
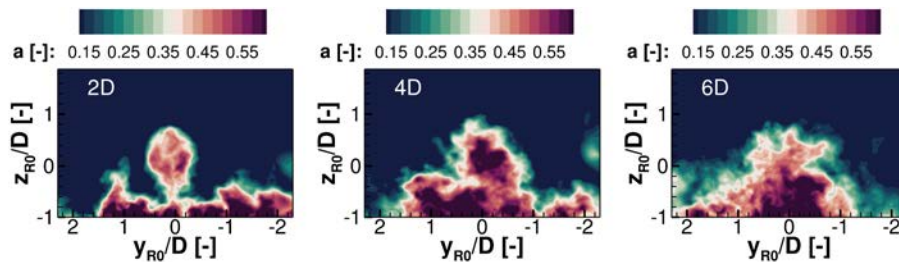
Figure 23. Comparison of the axial induction factors a in transverse planes of the wake 2D, 4D and 6D downstream of the wind turbine

downstream of the turbine, by both a and σ, the turbine wake is still distinguishable from the turbulent structures of the forest wake. This means at this position mixing is still relatively low. Further 2D downstream a mixing of the wake structures is already visible and the standard deviation σ depicts that the rotor induced fluctuations increase and occupy increasingly larger areas. In a distance 6D downstream of the turbine, forest wake and turbine wake have become a coherent structure. The standard deviation illustrates the decay of the wind turbine wake because

510
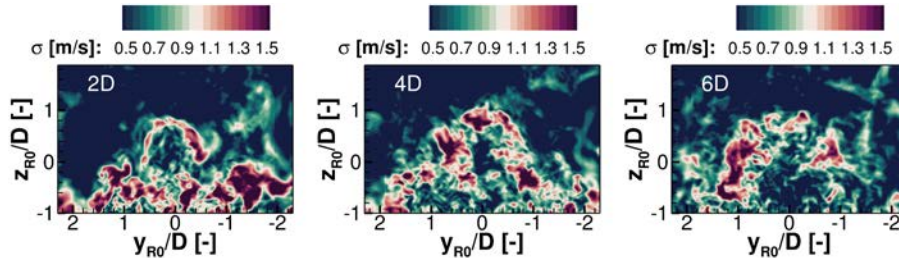
Figure 24. Comparison of the standard deviations σ in transverse planes of the wake 2D, 4D and 6D downstream of the wind turbine

the fluctuations propagate into extensive areas.

To analyse the combined topographic and meteorological influences on the wind turbine performance, simulation
515   results examining torque and torque fluctuations are presented below. For this purpose, the results were phase averaged over 25 revolutions.
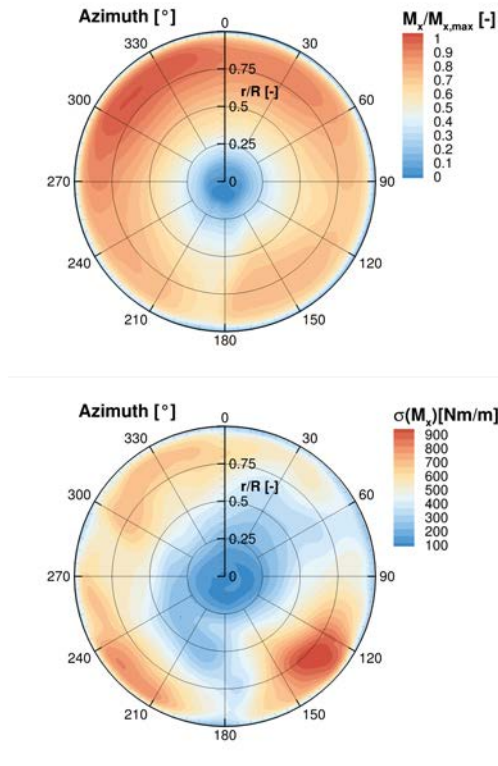
Figure 25. Distributions of the torque and of the standard deviation of the torque phase-averaged over 25 revolutions at the rotor plane

Figure 25 shows the phase-averaged torque distribution at the rotor plane, which is significantly responsible for generated power of the wind turbine. The upper plot depicts the phase averaged torque normalised by the maximum value. This maximum of the torque is reached in the upper-left area of the rotor plane. The maximum torque is generated between 290° and 340° because of the retreating blade effect. The escarpment of the orography and besides convective conditions with upwards acting buoyancy cause inclined flows. This upward wind increases the angle of attack at this position as the blade retreats in the left rotor half and advances in the right rotor half. The higher angles of attack increase the rotor loads and therefore the torque at this position. The forest wake causes lower torque to be generated in the lower half of the rotor, resulting in a power reduction. As can be interpreted from Fig. 20, the higher torque distributions of the upper rotor plane in contrast to the lower rotor plane do not result from the shear of the velocity profile, as this hardly changes over the rotor plane. The differences are rather due to the forest wake and the unstable conditions. At 180° the tower blockage causes lower values of M_x. To gain a better understanding of the effects of the turbulent flow field on the torque, the lower plot shows the standard deviation of the axial torque $\sigma(M_x)$. The largest torque fluctuations occur in the lower half of the rotor. As already described, turbulent vortices of the forest wake with reduced velocities flow across the lower half of the rotor plane, which leads to temporarily large velocity differences and therefore to high load fluctuations. The maximum of the torque fluctuations is reached between azimuth positions 120° and 150°. In this area the highest turbulent fluctuations occur as it was already analysed in the lower plot of Fig. 21. The increased load fluctuations arise across the entire lower half of the rotor. Because of the tower passage of the blade and the associated tower blockage, smaller torque fluctuations occur at 180°. Increased torque fluctuations also occur at the maximum rotor loads between 290° and 340°. The high ambient turbulence causes gusts that affect the inflow for this rotor position in the observed period. Many conditions affect the wind turbine at the test site. The orography leads to accelerations above the escarpment. The forest induces reduced velocities close to the ground, resulting in large shear effects and amplified turbulence. In addition, high turbulence intensities induced by the orography and convective flows have a strong impact on the wind turbine.

5   Conclusions

The paper presents the results of a study of highly resolved DDES simulations of a wind energy test site in complex terrain that is currently under construction in Southern Germany. In the first part of the results, the effects resulting from orography, forests, and thermal stratification were investigated and evaluated separately. Initially, the effects on the flow field were analysed and in a second step, the fully meshed wind turbine was integrated into the flow field. Subsequently, all effects were combined and applied to a real case study of 10 March 2021 in the second part of the results. The results of the simulated flow field were compared with met mast data. For the evaluation of this work, only comparative measurements of the wind field were available, as the construction of the turbines had not yet been completed on the test field at that time. Numerically, however, the wind turbine could be considered for
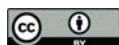
550   this period, which was subsequently also done in the results. The inflow, the wake and the performance output of
      the wind turbine were investigated. The main findings are listed below:

1) The escarpment accelerates the flow field at the altitude of the rotor plane. In combination with the upper
flow field that is less influenced by the orography, a boundary layer profile with low shear versus altitude results on
555   the plateau of the wind energy test site.

2) At the test site, the forest has a large impact on the flow field in ground proximity. Highly turbulent fluctu-
ations of low wind speeds in the forest wake strongly mix with the high velocity flow field above and result in highly
complex and turbulent flow situations.

560

3) Thermal stratification also has a strong impact on the ambient turbulence and the forest wake. Stable conditions
suppress turbulent mixing, especially downstream of the forested escarpment, whereas turbulence and dispersion are
strongly amplified for convective conditions.

565   4) By considering the wind turbine in the flow field, it has been shown that the forested escarpment impacts the
inflow of the turbine, as well as the mixing of the forest wake with the turbine wake. This affects wake decay further
downstream. Unstable conditions amplify this effect, while in stable conditions the wake extends further downstream.

5) Taking all these effects into account when simulating real conditions of a five-minute period on 10 March 2021,
570   decent agreements with the mean velocity profile and the turbulent statistics measured by the met masts were shown.

6) The prevailing unstable conditions led to increased mixing of the ambient turbulent flow with the forest wake.
This had an increased effect on the inflow of the rotor plane and on turbulence amplification in the forest wake.

575   7) To evaluate the performance output of a virtual turbine, all of these effects had to be considered. Topographic
effects and convective conditions cause low shear at the rotor position on the plateau. However, vortex structures
that detach from the forest occasionally cross the rotor plane and have a significant impact on performance in the
lower half of the rotor. Inclined flows in the escarpment are intensified by convective conditions, resulting in increas-
ing angles of attack and, therefore, more torque in the left rotor plane. The highly turbulent flow in the test field
580   also impacts the turbine rotor strongly.

This paper emphasised the importance of considering orography, vegetation, and thermal stratification in numerical
simulations to resolve the flow field decently. In this way, the effects on inflow, loads, power, and wake of the wind
turbine can also be predicted well.

585 *Data availability.* The raw data of the simulation results can be provided by contacting the corresponding author.

Author contributions. PL implemented the code extensions for the forest model and for thermal stratification, generated the entire preprocessing, performed the simulations, the analyses and evaluations of this work in the postprocessing and wrote the paper. GG generated the mesh of the wind turbine and built the setup for the turbine parameters. TL supported the research, defined and supervised the work, and revised the manuscript.

590 *Competing interests.* The authors declare that they have no conflict of interest.

Acknowledgements. This research is funded by the German Federal Ministry for Economic Affairs and Energy (BMWi) within the framework of the German joint research project "WINSENT" (Code number: 0324129). The authors gratefully acknowledge the support by the research network WindForS and acknowledge the provision of the computational resources of the High Performance Computing Center Stuttgart (HLRS) and the Leibniz Computing Center Munich (LRZ).

References

Abkar, M., Sharifi, A., and Porté-Agel, F.: Wake Flow in a Wind Farm during a Diurnal Cycle, Journal of Turbulence, 17, 1–22, https://doi.org/10.1080/14685248.2015.1127379, 2016.

Bangga, G., Weihing, P., Lutz, T., and Krämer, E.: Effect of computational grid on accurate prediction of a wind turbine rotor using delayed detached-eddy simulations, Journal of Mechanical Science and Technology, 31, 2359–2364, https://doi.org/10.1007/s12206-017-0432-6, 2017.

Barthelmie, R., Pryor, S., Wildmann, N., and Menke, R.: Wind Turbine Wake Characterization in Complex Terrain via integrated Doppler Lidar Data from the Perdigão Experiment, Journal of Physics: Conference Series, 1037, 052 022, https://doi.org/10.1088/1742-6596/1037/5/052022, 2018.

Bechmann, A. and Sørensen, N. N.: Hybrid RANS/LES Method for Wind Flow over Complex Terrain, Wind Energy, 13, 36–50, https://doi.org/https://doi.org/10.1002/we.346, 2010.

Belcher, S., Harman, I., and Finnigan, J.: The Wind in the Willows: Flows in Forest Canopies in Complex Terrain, Annual Review of Fluid Mechanics, 44, 479–504, https://doi.org/10.1146/annurev-fluid-120710-101036, 2012a.

Belcher, S. E., Harman, I. N., and Finnigan, J. J.: The Wind in the Willows: Flows in Forest Canopies in Complex Terrain, Annual Review of Fluid Mechanics, 44, 479–504, https://doi.org/10.1146/annurev-fluid-120710-101036, 2012b.

Benek, J. A., Steger, J. L., Dougherty, F. C., and Buning, P. G.: Chimera. A Grid-Embedding Technique, Tech. rep., AEDC-TR-85-64, Arnold Engineering Development Center, https://doi.org/https://doi.org/10.2514/6.1985-1523, 1986.

Berge, K. z., Schoen, M., Mauz, M., Platis, A., Kesteren, B. v., Leukauf, D., El Bahlouli, A., Letzgus, P., Knaus, H., and Bange, J.: A Two-Day Case Study: Comparison of Turbulence Data from an Unmanned Aircraft System with a Model Chain for Complex Terrain, Boundary-Layer Meteorology, https://doi.org/10.1007/s10546-021-00608-2, 2021.

Brodeur, P. and Masson, C.: Numerical Site Calibration over Complex Terrain, Journal of Solar Energy Engineering, 130, 031 020, https://doi.org/https://doi.org/10.1115/1.2931502, 2008.

Chougule, A., MANN, J., Kelly, M., and LARSEN, G.: Modeling Atmospheric Turbulence via Rapid-Distortion Theory: Spectral Tensor of Velocity and Buoyancy, Journal of the Atmospheric Sciences, 74, https://doi.org/10.1175/JAS-D-16-0215.1, 2016.

Churchfield, M. J., Lee, S., and Moriarty, P. J.: Adding Complex Terrain and Stable Atmospheric Condition Capability to the OpenFOAM-based Flow Solver of the Simulator for On/Offshore Wind Farm Applications (SOWFA), ITM Web of Conferences, 2, 02 001, https://doi.org/10.1051/itmconf/20140202001, 2014.

Desmond, C. J., Watson, S. J., and Hancock, P. E.: Modelling the Wind Energy Resource in Complex Terrain and Atmospheres. Numerical Simulation and Wind Tunnel Investigation of non-Neutral Forest Canopy Flow, Journal of Wind Engineering and Industrial Aerodynamics, 166, 48–60, https://doi.org/https://doi.org/10.1016/j.jweia.2017.03.014, 2017.

Dupont, S., Brunet, Y., and Finnigan, J. J.: Large-Eddy Simulation of Turbulent Flow over a Forested Hill: Validation and Coherent Structure Identification, Quarterly Journal of the Royal Meteorological Society, 134, 1911–1929, https://doi.org/https://doi.org/10.1002/qj.328, 2008.

El Bahlouli, A., Leukauf, D., Platis, A., zum Berge, K., Bange, J., and Knaus, H.: Validating CFD Predictions of Flow over an Escarpment Using Ground-Based and Airborne Measurement Devices, Energies, 13, https://doi.org/10.3390/en13184688, 2020.

Emeis, S.: Wind energy meteorology : atmospheric physics for wind power generation, Green Energy and Technology, Springer Verlag, 12.02.03; LK 01, 2013.

Finnigan, J., Ayotte, K., Harman, I., Katul, G., Oldroyd, H., Patton, E., Poggi, D., Ross, A., and Tay-
635   lor, P.: Boundary-Layer Flow Over Complex Topography, Boundary-Layer Meteorology, 177, 247 – 313, https://doi.org/https://doi.org/10.1007/s10546-020-00564-3, 2020.

ForstBW: Schwäbische Alb, https://www.forstbw.de/wald-im-land/zahlenwunder/strukturen/wuchsgebiete/ schwaebische-alb/, access date:23.02.2021, 2021.

Guma, G., Bangga, G., Schwarz, E., Lutz, T., and Krämer, E.: Consistent 3D CFD and BEM simulations of a research turbine
640   considering rotational augmentation, Journal of Physics: Conference Series, 1037, 022 024, https://doi.org/10.1088/1742-6596/1037/2/022024, 2018.

Guma, G., Bangga, G., Lutz, T., and Krämer, E.: Aero-elastic analysis of wind turbines under turbulent inflow conditions, https://doi.org/10.5194/wes-2020-22, 2020.

Ivanell, S., Arnqvist, J., Avila, M., Cavar, D., Chavez-Arroyo, R. A., Olivares-Espinosa, H., Peralta, C., Adib, J., and Witha,
645   B.: Micro-scale model comparison (benchmark) at the moderately complex forested site Ryningsnäs, Wind Energy Science, 3, 929–946, https://doi.org/10.5194/wes-3-929-2018, 2018.

Jameson, A., Schmidt, W., and Turkel, E.: Numerical Solution of the Euler Equations by Finite Volume Methods Using Runge-Kutta Time Stepping Schemes, AIAA Paper, 81, https://doi.org/10.2514/6.1981-1259, 1981.

Keck, R.-E., Veldkamp, D., Wedel-Heinen, J., and Forsberg, J.: A consistent turbulence formulation for the dynamic wake
650   meandering model in the atmospheric boundary layer, no. 0012(EN) in DTU Wind Energy PhD, DTU Wind Energy, Denmark, 2013.

Kroll, N., Rossow, C.-C., Becker, K., and Thiele, F.: The MEGAFLOW Project, Aerospace Science and Technology, 4, 223–237, https://doi.org/https://doi.org/10.1016/S1270-9638(00)00131-0, 2000.

Letzgus, P., Lutz, T., and Krämer, E.: Detached Eddy Simulations of the local Atmospheric Flow Field within a
655   Forested Wind Energy Test Site located in Complex Terrain, Journal of Physics: Conference Series, 1037, 072 043, https://doi.org/10.1088/1742-6596/1037/7/072043, 2018.

Letzgus, P., Bahlouli, A. E., Leukauf, D., Hofsäß, M., Lutz, T., and Krämer, E.: Microscale CFD Simulations of a Wind Energy Test Site in the Swabian Alps with Mesoscale Based Inflow Data, Journal of Physics: Conference Series, 1618, 062 021, https://doi.org/10.1088/1742-6596/1618/6/062021, 2020.

660   Mann, J.: The spatial structure of neutral atmospheric surface layer turbulence, Journal of Fluid Mechanics, 273, 141–168, https://doi.org/10.1017/S0022112094001886, 1994.

Mann, J.: Wind field simulation, Probabilistic Engineering Mechanics, 13, 269–282, https://doi.org/10.1016/S0266-8920(97)00036-2, 1998.

Menter, F.: Two-Equation Eddy-Viscosity Turbulence Models for Engineering Applications, AIAA journal, 32, 1598–1605,
665   https://doi.org/https://doi.org/10.2514/3.12149, 1994.

Müller, J., Lutz, T., and Krämer, E.: Numerical Simulation of the Swept FNG Wing in Atmospheric Turbulence, AIAA AVIATION 2020 FORUM, https://doi.org/https://doi.org/10.2514/6.2020-2778, 2020.

Murphy, P., Lundquist, J. K., and Fleming, P.: How wind speed shear and directional veer affect the power production of
a megawatt-scale operational wind turbine, Wind Energy Science, 5, 1169–1190, https://doi.org/10.5194/wes-5-1169-2020,
670   2020.

Peña, A., Gryning, S.-E., and Mann, J.: On the Length-Scale of the Wind profile, Quarterly Journal of the Royal Meteorological
Society, 136, 2119–2131, https://doi.org/https://doi.org/10.1002/qj.714, 2010.

Radünz, W. C., Sakagami, Y., Haas, R., Petry, A. P., Passos, J. C., Miqueletti, M., and Dias, E.: Influ-
ence of Atmospheric Stability on Wind Farm Performance in Complex Terrain, Applied Energy, 282, 116 149,
675   https://doi.org/10.1016/j.apenergy.2020.116149, 2021.

Sathe, A., Mann, J., Barlas, T., Bierbooms, W., and van Bussel, G.: Influence of atmospheric stability on wind turbine loads,
Wind Energy, 16, https://doi.org/10.1002/we.1528, 2013.

Schäferlein, U., Keßler, M., and Krämer, E.: High Order CFD-Simulation of the Rotor-Fuselage Interaction, 39th European
Rotorcraft Forum, pp. 37–39, 2013.

680   Schubiger, A., Barber, S., and Nordborg, H.: Evaluation of the lattice Boltzmann method for wind modelling in complex
terrain, Wind Energy Science, 5, 1507–1519, https://doi.org/10.5194/wes-5-1507-2020, 2020.

Schulz, C., Hofsäß, M., Anger, J., Rautenberg, A., Lutz, T., Cheng, P. W., and Bange, J.: Comparison of Different Mea-
surement Techniques and a CFD Simulation in Complex Terrain, Journal of Physics: Conference Series, 753, 082 017,
https://doi.org/101088/1742-6596/753/8/082017, 2016.

685   Shaw, R. H. and Schumann, U.: Large-eddy Simulation of Turbulent Flow above and within a Forest, Boundary-Layer
Meteorology, 61, 47–64, https://doi.org/10.1007/BF02033994, 1992.

Troldborg, M., Sorensen, n., Norkaer, J., and Mikkelsen, R, F.: Actuator Line Modeling of Wind Turbine Wakes, Dissertation,
2008.

Troldborg, N., Sørensen, J., Mikkelsen, R., and Sørensen, N.: A Simple Atmospheric Boundary Layer Model applied to Large
690   Eddy Simulation of Wind Turbine Wakes, Wind Energy, 17, https://doi.org/10.1002/we.1608, 2014.

Wegley, H. L., Ramsdell, J. V., Orgill, M. M., and Drake, R. L.: Siting Handbook for Small Wind Energy Conversion Systems,
Battelle Pacific Northwest Labs., Richland, WA (USA), https://doi.org/10.2172/5490541, 1980.

Weihing, P., Letzgus, J., Bangga, G., Lutz, T., and Krämer, E.: Hybrid RANS/LES capabilities of the flow solver
FLOWer—Application to flow around wind turbines, vol. 137, pp. 369–380, https://doi.org/10.1007/978-3-319-70031-1_31,
695   2018.